NRC Publications Archive
Archives des publications du CNRC

An advantageous imaging perspective for quantitative evaluation of 7075 aluminum alloy grain boundary precipitates using scanning electron microscope

Li, Dong; Tu, Siyu; Chen, Jian; Gagné, Marc-Olivier

This publication could be one of several versions: author's original, accepted manuscript or the publisher's version. / La version de cette publication peut être l'une des suivantes : la version prépublication de l'auteur, la version acceptée du manuscrit ou la version de l'éditeur.
For the publisher's version, please access the DOI link below./ Pour consulter la version de l'éditeur, utilisez le lien DOI ci-dessous.

Publisher's version / Version de l'éditeur:
https://doi.org/10.1002/jemt.24117
Microscopy Research and Technique, 2022-04-05

NRC Publications Archive Record / Notice des Archives des publications du CNRC :
https://nrc-publications.canada.ca/eng/view/object/?id=9890e04b-6d8f-451e-80db-3dbe10b9de25
https://publications-cnrc.canada.ca/fra/voir/objet/?id=9890e04b-6d8f-451e-80db-3dbe10b9de25

Access and use of this website and the material on it are subject to the Terms and Conditions set forth at
https://nrc-publications.canada.ca/eng/copyright
READ THESE TERMS AND CONDITIONS CAREFULLY BEFORE USING THIS WEBSITE.

L'accès à ce site Web et l'utilisation de son contenu sont assujettis aux conditions présentées dans le site
https://publications-cnrc.canada.ca/fra/droits
LISEZ CES CONDITIONS ATTENTIVEMENT AVANT D'UTILISER CE SITE WEB.

Questions? Contact the NRC Publications Archive team at
PublicationsArchive-ArchivesPublications@nrc-cnrc.gc.ca. If you wish to email the authors directly, please see the first page of the publication for their contact information.

Vous avez des questions? Nous pouvons vous aider. Pour communiquer directement avec un auteur, consultez la première page de la revue dans laquelle son article a été publié afin de trouver ses coordonnées. Si vous n'arrivez pas à les repérer, communiquez avec nous à PublicationsArchive-ArchivesPublications@nrc-cnrc.gc.ca.

An advantageous imaging perspective for quantitative evaluation of 7075 Aluminum alloy grain boundary precipitates using scanning electron microscope

Dong Li, Siyu Tu, Jian Chen, Marc-Olivier Gagné
National Research Council of Canada - Aluminum Technology Centre, Saguenay (Qc.), Canada, G7H 8C3

Correspondence should be addressed to

501 Boulevard l'Université, Saguenay, Québec, Canada, G7H 8C3

Siyu Tu: Siyu.Tu@cnrc-nrc.gc.ca Tel : +1 418-545-5397

Keywords: microstructure analysis, backscattered electron, stress corrosion cracking

Abstract

7075 Aluminum alloy (AA7075) samples undergone four aging sequences were examined using a scanning electron microscope (SEM) and a transmitted electron microscope (TEM). The measurements results validate the correlation between stress corrosion cracking (SCC) resistance and the size and inter-distance of the grain boundary precipitates (GBPs). To evaluate the size and inter-distance of GBPs, we demonstrate in this study a highly efficient SEM imaging technique that can unfold grain boundary in a two-dimensional view. Compared to TEM, imaging with backscattered electrons in SEM (SEM-BSE) is more advantageous for GBPs presentation and measurements. The major reason is that about 900 times more sampling area can be imaged with SEM from the same specimen for TEM observation, thus enabling frequent appearances of GBPs at normal top view perspective, a planar view best for GBPs quantitative analysis but not well-documented. The acceleration tension of SEM for imaging was optimized at 10 kV with an information depth of around 330 nm.

Research highlights:

- SEM imaging using backscattered electrons is efficient for AA7075 grain boundary precipitate imaging.
- The precipitate size and inter-distance can be more accurately measured with the perspective of normal top view under SEM than TEM.

Graphical Abstract:

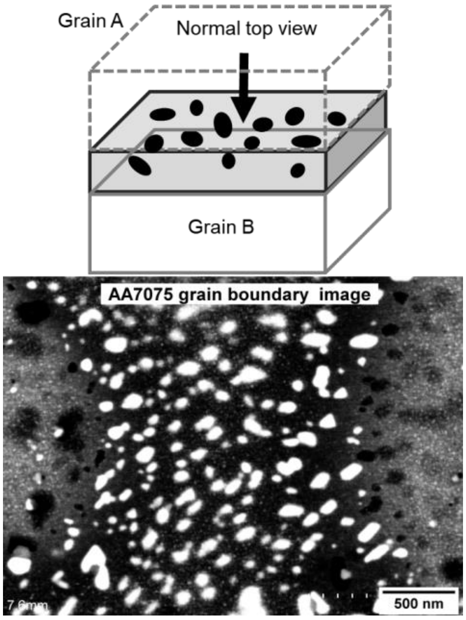

1. Introduction

The Al-Zn-Mg-Cu (7xxx) type alloys have a long history of application in the aerospace industry and are increasingly applied in the automotive industry nowadays because of their high strength and light-weight (Mondolfo, 1971; Polmear et al., 2017; Starink, 2001). Their strength can even match many grades of steels due to the coherent/semicoherent nano-scale η''/η'-$MgZn_2$ precipitates in the matrix produced during aging treatment (Deshpande et al., 1998; Ghosh et al., 2020) or in-process cooling (Kumar et al., 2017, 2018, 2021). However, 7xxx series of Al alloy are susceptible to SCC (Ajay Krishnan et al., 2018; Bobby-Kannan et al., 2003; Burns et al., 2010; Kannan et al., 2004). The GBPs within the precipitation free zones (PFZs), mainly η-$Mg(Zn,Cu,Al)_2$, play an important role in initiating the SCC because they are anodic to the PFZs and preferentially undergo severe dealloying, especially in NaCl environments (Ajay Krishnan et al., 2018; Knight et al., 2010; Liu et al., 2015; Prabhuraj et al., 2017) The size, inter-distance and chemical composition of GBPs are some of the key parameters that control the SCC process (Huang et al., 2012; Kannan & Raja, 2006; Knight et al., 2010, 2015; Liu et al., 2015; Peng et al., 2011). Conventionally we use a TEM to fully characterize the microstructure of grain boundary and precipitates (Huang et al., 2012; Kannan & Raja, 2006; Zhou et al., 2021).

There are considerable reports on SCC behaviors varying with GBPs microstructure as well as chemical composition produced under different aging (retrogression and re-aging) and quenching treatments (Goswami et al., 2013; Liu et al., 2015). It has been widely accepted that the Cu-rich, discrete and coarse GBPs are beneficial to the corrosion resistance of 7xxx alloys (Birbilis & Buchheit, 2005; Huang et al., 2012; Kannan & Raja, 2006; Knight et al., 2015; Peng et al., 2011). However, large PFZs area fraction under low quenching rate is suspected to contribute to their rapid corrosion (Liu et al., 2015). Furthermore, little correlation between SCC resistance and grain-boundary/matrix microstructures in 7xxx alloys has also been claimed in some literature (Knight et al., 2010, 2015).

To systematically study and compare the importance of factors influencing the SCC resistance, reliable, fast, and accurate characterization methods are of vital importance. However, there are limited tools to observe the GBPs microstructures. Although TEM is the most popular tool for GBPs observation bringing high resolution images with excellent contrast (Ajay Krishnan et al., 2018; Kannan & Raja, 2006; Zhou et al., 2021), there exist some limitations. First, the most adopted sample preparation method for AA7075 TEM observation - electropolishing - is sensitive to the variation of experimental parameters (i.e., voltage, current density, temperature, time, and flow rate), characteristics (thickness, conductivity, etc.) of the specimen (Ünlü, 2008) and is also highly dependent on the experience of the operator. The observable area is frequently limited to a small region depending on the quality of electropolishing. Several samples are usually prepared to guarantee a sufficient sampling area. Second, a TEM image is a projection where numerous precipitates in a three-dimensional sample are projected into a two-dimensional field of view, overlapping each other and hindering the ability to be properly quantified for their size and inter-distance. Third, the thickness of the specimen varies from spot to spot caused by electropolishing. The quantification of precipitates thus requires thickness measurements at each spot to normalize the effect of overlapping, which is time-consuming. Last but not least, the TEM is, in general, less accessible thus more expensive to produce results at scale compared to SEM, which limits the potential of mass production of images for data analytics.

To tackle every pain point mentioned above, in this paper we propose an advantageous SEM imaging technique using backscattered electrons (BSE) with the perspective of normal top view (Fig. 1) to produce representative results of size and inter-distance of precipitates at grain boundaries in AA7075. TEM images were acquired in the direction of parallel lateral view (Fig. 1) in contrast to demonstrate the ineffectiveness when accessing some of the GBPs measurements, notably the inter-distance of precipitates. SEM imaging conditions have been optimized with Monte Carlo simulations to understand the visibility and contrast of precipitates. SEM-BSE imaging has also been compared with TEM imaging, notably in high angle annular dark-field scanning transmitted electron microscope (HAADF-STEM) mode, with the perspective close to normal top view for GBPs observation. Finally, the correlation between the characterized GBPs microstructure and the SCC resistance has been studied for AA7075 samples respectively after four different heat-treatments.

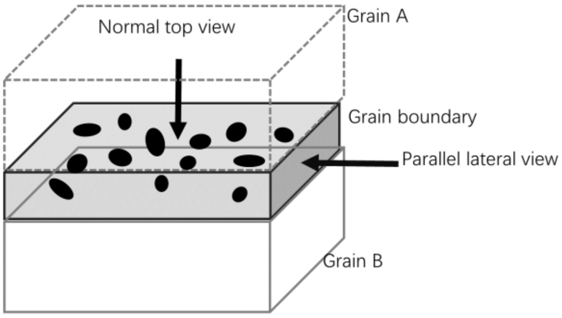

Fig. 1 Scheme of perspectives with normal top view and parallel lateral view to observe grain boundaries.

2. Materials and methods

An AA7075 type alloy in the form of a 2 mm as-rolled sheet was prepared with four different temper methods, named T6, temper-A, T73, and temper-B respectively (Table 1.). A JEM2200FS with Schottky field emission source TEM operating at 200 kV, and a Hitachi Su-70 Schottky field emission SEM were used to observe the grain boundary microstructures for the comparison of each sample. Monte Carlo simulations of backscattered electrons based on the SEM were performed using Casino v2.51 (Drouin et al., 2007), with boost software license 1.0. Image analysis of grain boundary microstructure, including precipitates identification and localization, was carried out using ImageJ with the license of open-source software projects. The nearest neighbor distance was calculated using Python 3.8 under the PSF License Agreement and the Zero-Clause BSD license.

Table 1. Artificial aging heat treatments applied to the AA7075 alloy.

Artificial aging treatment	**Aging sequence**
T6	120°C/24 h
temper-A*	121°C/1 h + 177°C/1.5 h
T73	107°C/6 h + 162°C/24 h
temper-B	Proprietary information

*based on the reference (Berg et al., 2001).

Each TEM sample was electropolished using a Struers® twin-jet electropolisher at 12 V for 2-5 min in a mixture of 67 % methanol and 33 % concentrated HNO_3, at a temperature of approximately -30°C. The prepared TEM samples were directly used for SEM imaging.

U-bend specimens for stress-corrosion cracking evaluation were prepared in accordance with ASTM G30-97 *Standard Practice for Making and Using U-Bend Stress-Corrosion Test Specimens*. They were prepared as 150 mm by 25 mm coupons with the length perpendicular to the rolling direction. The outer surface and edges were mechanically polished and degreased with acetone prior to the test. A two-stage stressing method was applied to ensure that the specimen remained in a state of plastic deformation. The SCC experiment consisted of an alternate immersion at room temperature (~ 20°C, 30-40% relative humidity): 10 min immersion followed by a drying period of

1h50. The total duration of the test was 1848h (924 cycles). The solution used for the SCC evaluation is to represent the de-icing salts used on the roads during winter in North America. It was prepared to simulate a realistic corrosion environment encountered in the automotive industry. The electrolyte was prepared with deionized water and its composition is detailed in table 2. The specimens were inspected daily and the time to failure was recorded correspond to the difference of time between the beginning of the exposure and the first observation of a crack.

Table 2. Electrolyte composition used for SCC experiment.

Component	Concentration (% m/m)
NaCl	5.13
Na_2SO_4	0.202
$CaCl_2$	0.151

3. Results and discussion

3.1 Parallel lateral view of grain boundaries by TEM and SEM

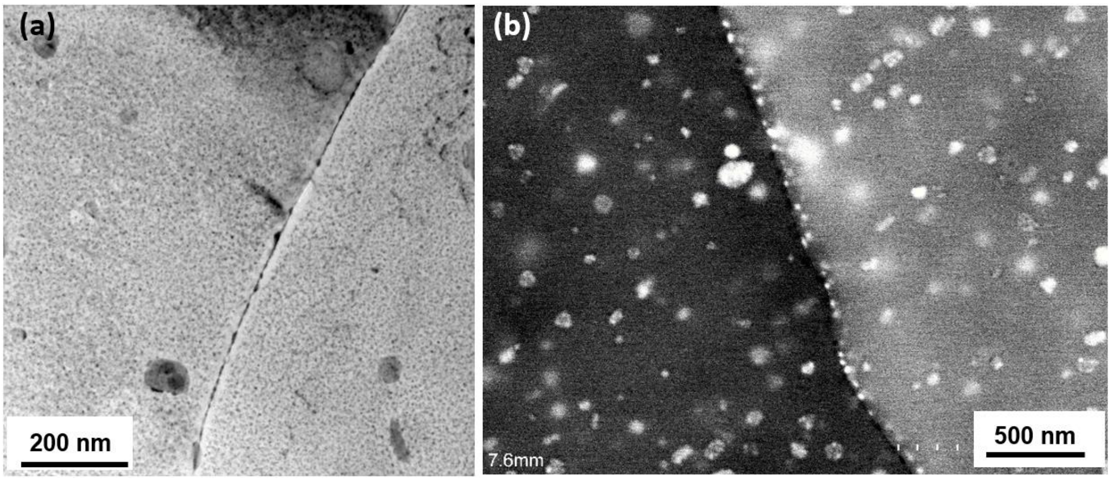

Fig. 2 (a) TEM image of GBPs of AA7075 at T6 temper from parallel lateral view. (b) SEM-BSE image of GBPs of AA7075 at T6 temper from lateral view.

The parallel lateral view of grain boundary, illustrated in Fig. 1, is the most frequent observation direction reported in the literature (Huang et al., 2012; Kannan & Raja, 2006; Peng et al., 2011; Zhou et al., 2021). Clear projection of PFZ facilitates the interpretation of grain positions and the accurate measurements of PFZ width. Besides, the GBPs aligned one by one in the middle of PFZ are well separated from the rest of the precipitates in the matrix, which is of aesthetic sense and avoids overlapping between GBPs and precipitates in the matrix.

By tilting the sample in one or two orthogonal directions in TEM, we can measure the PFZ width. When the PFZ is tilted to be parallel to the incident electron beam, it appears clearly in the TEM image as shown in Fig. 2(a) with both edges defined by the absence of hardening precipitates. In contrast, SEM fails to offer such clarity mainly due to higher electron interaction volume, which leads to a lower spatial resolution of hardening precipitates in the matrix and the overlapping of the matrices over and beneath the grain boundary. SEM-BSE image shown in Fig. 2(b) was acquired with a lateral view of PFZ, but since the GBPs are not aligned perfectly and some of them are adjacent, expanding the width of the boundary line, this boundary is close, but not completely parallel to the incident beam. With a sub-hundred nm thickness in transmission mode, the TEM observation can guarantee that the parallel state of the boundary to incident beam is achieved. Whereas in SEM, it is more difficult to really confirm the parallel state with a visible depth of several hundred nanometers. Therefore, it is preferable to measure the PFZ width using TEM.

Fig 2(a) shows an optimum tilting position for PFZ width measurement. In practice, however, such tilting can introduce some inconveniences. First, it increases the thickness of the probing area, which decreases the contrast and resolution. Second, the employed TEM only allows a ±40° tilting angle range due to the limitation of the sample holder, which limits the grain boundaries that are able to be tilted to the ideal orientation. The example in Fig. 3 demonstrates that a 36° tilting of the primary axis was applied before the GBPs were regressed to a single line. Third, the tilting may also bring diffraction contrast which influences the image quality, as shown in Fig. 3. Moreover, with randomly oriented grain boundaries, it is difficult to tell if one boundary is a candidate for the PFZ measurements before tilting. Despite these inconveniences, the parallel lateral view with TEM imaging is still the method to choose for PFZ width measurement, given the excellent contrast and clear definition of PFZ edge.

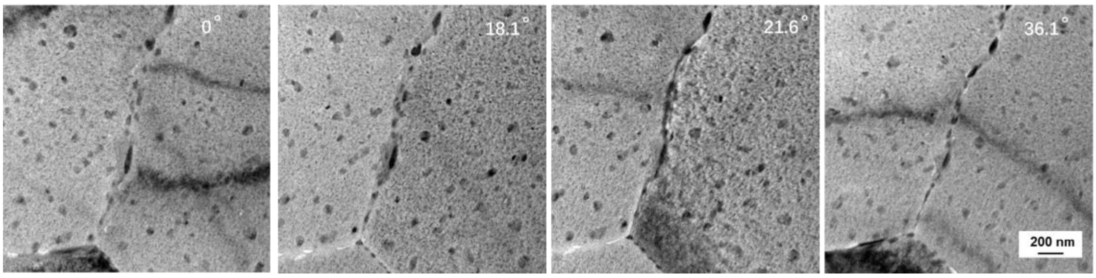

Fig. 3 Grain boundary microstructure of AA7075 with T73 temper under TEM with a step-by-step tilt.

Nevertheless, it is difficult to perform the size and inter-distance measurements for GBPs using TEM images with the perspective of parallel lateral view. In Fig. 2(a), the GBPs are present as a form of one line and they overlap each other in projection, which makes it impossible to access their size, shape, and inter-distance. The overlapping of GBPs is not present in Fig. 2(b) and the GBPs are present separately in a line or a region. This is mainly due to the observed PFZ not being completely parallel to the beam. The GBPs at a greater depth within such PFZ generate a lower intensity of signal than the GBPs at a smaller depth. Given the clear definition of individual GBPs in SEM-BSE images of the T6 sample, it is possible to measure the size and inter-distance of GBPs. However, it is still not ideal to measure the inter-distance using SEM-BSE in the direction of lateral view for two main reasons. First, the distance between precipitates within the grain boundary in Fig. 2(b) is only the distance along the boundary direction but not the nearest neighbor distance. Second, from the perspective of lateral view, only one line of GBPs per PFZ is available for quantitative analysis whereas the grain boundary is a two-dimensional plane with much more GBPs. The following section introduces the normal top view of grain boundary by SEM-BSE to solve these two issues.

3.2 Normal top view of grain boundaries by SEM-BSE and TEM

The comparison between TEM and SEM imaging for grain boundary of AA7075 in the previous section is mainly focused on the perspective of grain boundary parallel to the incident beam (parallel lateral view). When the angle is high between grain boundary and incident electron beam, the hardening precipitates within the grain above and below the grain boundary are projected into the two-dimensional plane where the TEM image is collected. The mixed contrast of bend contour, thickness variation as well as overlapping of precipitates has a negative effect on the GBPs observation. Moreover, the limited imaging area brings extra difficulties to obtain accurate quantitative information of GBPs. However, the imaging using SEM-BSE does not have such issues. Without any sample tilting, regions can be found due to a large observation area where the grain boundaries are nearly perpendicular to the incident beam. This particular viewing angle of GBPs is termed as normal top view in this paper. The following section details the application of SEM-BSE for grain boundary normal top view imaging.

3.2.1 Monte Carlo simulation of depth and voltage - visibility study of SEM-BSE

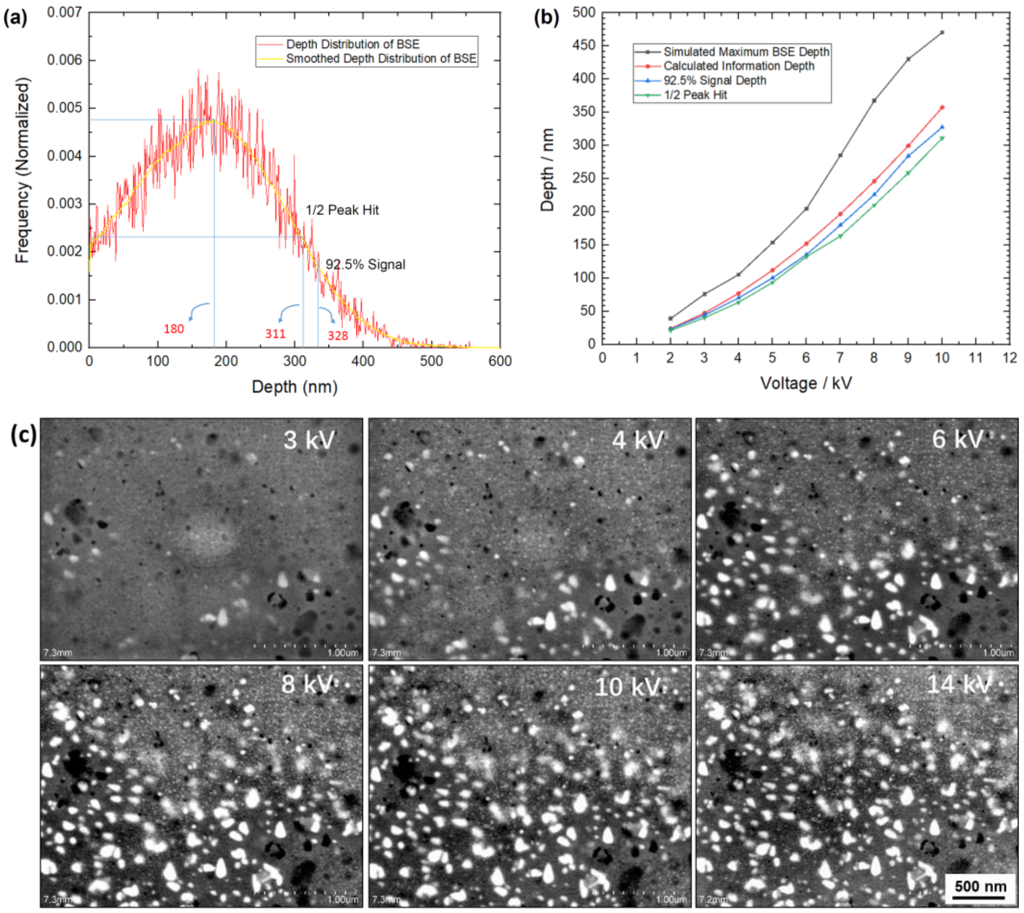

Fig. 4 (a) Depth distribution function of electron hits at 10kV. (b) Simulated BSE signal depth as a function of acceleration tension. (c) SEM-BSE images showing visibility vs. acceleration tension.

The energy of BSE is usually ranging from 50 eV to nearly the incident beam energy, and the incident electrons elastically scatter and leave the sample to show sub-surface signals(Mullerova & Frank, 2003). Under the backscattered electron mode, the alloying elements with larger atomic number Z (Zn and Cu) in GBPs render higher contrast in Al matrix. To achieve even higher contrast for high atomic number elements, it is preferable to move the sample closer to the detector, since BSE at a wide scattering angle are not captured when moving the sample further away from the detector (Richards et al., 2000). In terms of spatial resolution, a relatively small working distance is also beneficial to SEM-BSE imaging. The SEM images achieved in Fig. 2(b) look similar to STEM images shown in the literature (Kairy et al., 2018; Zhou et al., 2021).

The Monte Carlo simulations have been conducted by using Casino software (Drouin et al., 2007) to estimate the distribution of backscattered electrons under different voltages. 10^5 electrons were simulated for each voltage step to calculate the depth distribution function (DDF) of the backscattered electrons as shown in Fig. 4(a). The electrons that come from maximum depth, counting for less than a tenth of the signal, do not contribute much to the imaging.

Plenty of studies have developed different models to estimate the penetration depth and information depth (ID) of electrons (Assa'd & Gomati, 1998; Kanaya & Okayama, 1972; PiŇos et al., 2017). ID is the distance from the surface to the deep element of the structure that can be just imaged (Niedrig & Rau, 1998). In some studies, ID has been simply taken as a fraction of its penetration depth (Frank et al., 2000; Rau & Reimer, 2001; Richards et al., 2000). A modified theoretical equation based on Kanaya and Okayama's work (Kanaya & Okayama, 1972) was reported (PiŇos et al., 2017) as

$$\mathrm{ID}_{BSE} = \frac{7.5AE^{1.67}}{\rho Z^{0.89}}$$

, where ID_{BSE} (nm) is the information depth of the BSE; A is the atomic weight; Z is the atomic number; E is the energy of incident electrons and ρ is the density of the target. The ID can also be determined based on emission DDF for the signal of interest. PiŇos et al. in their study recommended the ID as a depth within which 92%-93% of the signal generated (PiŇos et al., 2017), though the standards (ISO18115 and ASTM E-42) define 95% or 99% as the suitable threshold. Another empirical method estimating the ID is to put the threshold halfway down the falling slope in the DDF (PiŇos et al., 2017). As can be seen in Fig. 4(b), the methods to estimate the ID have slight differences (red, blue, and green lines). We estimate with a 92.5% generated signal that the ID is around 330 nm at 10kV for AA7075, as illustrated in Fig. 4(a).

An area of PFZ from the AA7075 temper-B was selected to visualize the influence of acceleration tension on the visibility of GBPs, shown in Fig. 4(c). At 3 kV voltage, the average depth of backscattered electrons is only around 46 nm. The difference between the backscattered electron coefficient (η) of Al and heavier Cu/Zn is relatively small at 3 kV, which results in low contrast. Therefore, only some corrosion pits on the surface are revealed with some shallow precipitates appearing at the surrounding of the concave. As the tension increases, more precipitates are revealed as shown in Fig. 4(c) from 4 kV to 10 kV. The contrast also becomes better for precipitates in lower depth because the η of Al decreases while the η of Cu/Zn increases with the increase of electron beam energy (Assa'd & Gomati, 1998; Frank et al., 2000). At around 8~10 kV, all of the GBPs at the bottom left region in the field of view are revealed. However, higher tension does not help reveal more GBPs in the region because the PFZ is fully penetrated and therefore excessive voltage will only introduce the fine matrix precipitates underneath into the image, which brightens the background and reduces the contrast of the image. It is to note that the grain boundary expands towards the top right region in the field of view from 6 kV to 14 kV, which suggests that this PFZ is deeper at the top right compared to the bottom left region. Therefore, in this grain boundary, most of the GBPs are distributed at the level of depth with ID from 4 kV to 10 kV, namely between 75 nm to 330 nm approximately.

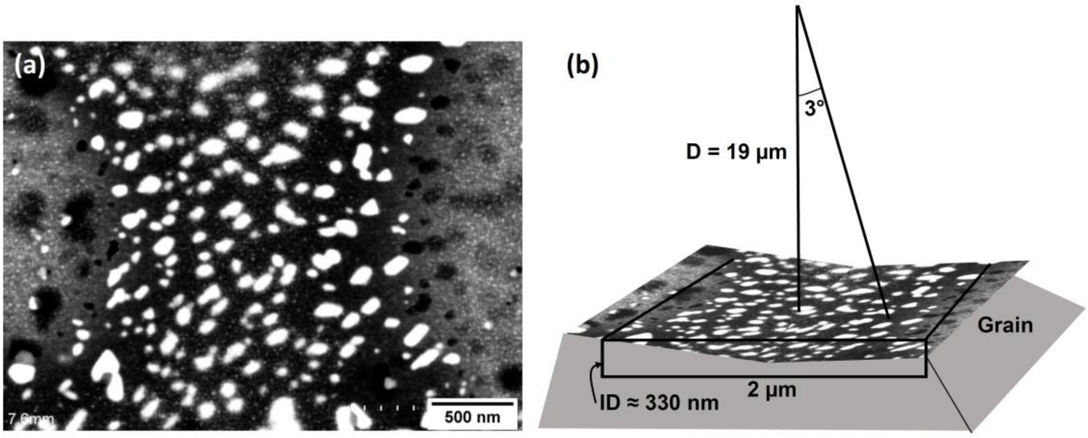

Fig. 5 SEM-BSE image (a) and illustration (b) of a concave grain boundary with ID at 10 kV.

Fig. 5(a) shows an SEM-BSE image of a grain boundary section with a width of around 2 μm. GBPs at two edges are etched out with visible holes (contrast in black) in the image. Since the etching happens at the surface during electropolishing, such appearance corresponds to a concave structure of the boundary, illustrated in Fig. 5(b). The average grain equivalent diameter measured by EBSD is around 24 μm. If we assume the grain is a 24 μm diameter sphere, given the symmetry of this concave boundary structure and 2 μm width, the angle between the surface and the boundary is less than 3°. However, the EBSD mapping in Fig. S1 reveals that the grains are nonspherical and the sizes vary drastically from one grain to another (details in supporting information). It is possible that this grain is smaller, of which the boundary is more curved. Nevertheless, the information depth at 10 kV confines the maximum depth of the GBPs in the image – 330 nm. Given the concave boundary structure of 2 μm width, it is still reasonable to approximate at the center an area parallel to the surface that is suitable for measurements of GBPs size and inter-distance. In fact, given a fixed acceleration tension, the larger the area of spread GBPs appears in the field of view, the higher chance a flat grain boundary is observed. Even though in most cases SEM-BSE images from normal top view do not show completely flat surfaces of PFZ, this observation direction with high contrast and large boundary area still enables us to measure the GBPs size and inter-distance, providing more data per image with better accuracy than measurements using TEM images with the perspective of parallel lateral view. Empirically, we consider an area of a circle with a 2 μm diameter to be flat enough for GBPs measurements at 10 kV acceleration voltage.

3.2.2 Comparison of SEM-BSE and TEM in normal top view

As discussed in previous sections, the TEM bright-field images of PFZ are usually in parallel lateral view direction for their high resolution and clear definition of PFZ border and GBPs inside. However, it is difficult to conduct TEM observation for normal top view imaging for two main reasons. First, the suitable thickness of the Al alloy sample for TEM observation at 200 kV is less than 100 nm, which leads to much fewer opportunities to encounter a grain boundary considered to be flat enough to perform the observation with the perspective of normal top view. Usually, only a small section of the boundary plane appears as the intersection with the observed volume of sub-100 nm in thickness, as shown in Fig. 6(a), similar to what we can observe with SEM-BSE in Fig. 4(c) at 4 kV (ID ~75 nm). Second, the diffraction contrast of bend contour will further influence the quality of the image, hindering the accuracy of measurements for GBPs, as shown in Fig. 3 at 0° and in Fig. 6(a) at 14.1°. A study suggests that the HAADF-STEM can generate images less prone to the two concerns above. Bend-contour-free images at a relatively higher thickness (> 200 nm) can be imaged with decent contrast and resolution (Zhu et al., 2018).

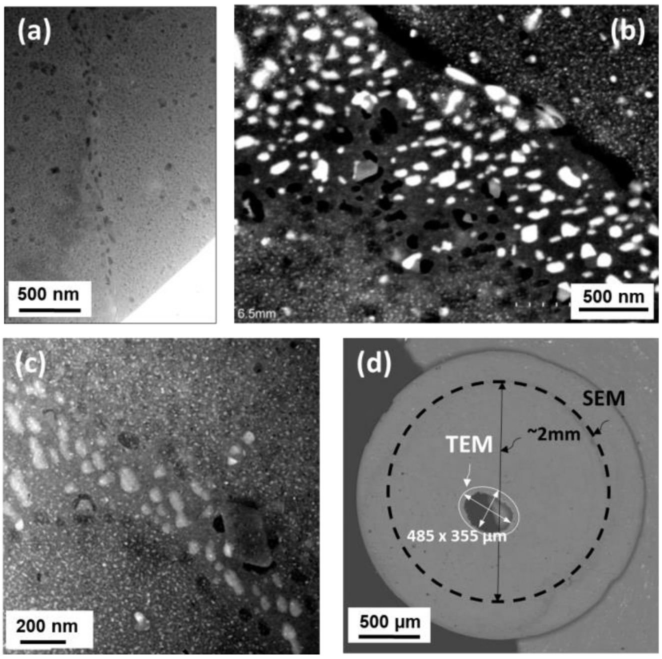

Fig. 6 (a)TEM bright-field (b)SEM-BSE and (c)HAADF-STEM image of AA7075 grain boundary at T73 temper with perspectives close to normal top view; (d) SEM image of 3 mm diameter AA7075 disc at T73 temper with an electropolished hole of 485 × 355 µm, demonstrating the difference of observable area between TEM and SEM for the same sample.

Fig. 6 (a,b,c) shows images of AA7075 grain boundaries at T73 temper acquired by TEM, SEM, and HAADF-STEM respectively. Due to the thinness of the sample, the TEM image of grain boundary in Fig. 6(a) appears narrower than what was observed with SEM-BSE as shown in Fig 6(b). Moreover, the precipitates shown in TEM bright-field image seem to be smaller (around 50 nm) than those in the SEM image (some over 150 nm) while they come from the same specimen. It is highly likely that the thickness near the hole in Fig. 6(a) is less than 100 nm, which automatically excludes the precipitates with larger size. Therefore, the GBPs sizes are underestimated using TEM in areas with thickness less than 100 nm. This effect is less obvious with HAADF-STEM imaging (Fig. 6 (c)) because as mentioned above the thickness can be larger (~200 nm) without image deterioration (Zhu et al., 2018). The HAADF-STEM image is close to the one shown in the SEM-BSE image (Fig. 6 (b)). Thanks to a converged beam scanning the area, the bend contour is not present. Compared to TEM bright-field image, the HAADF-STEM is a better alternative to measure the GBPs size and inter-distance.

The resolution of HAADF-STEM image is in general better than SEM-BSE image but the contrast of GBPs is not as good. Compared to SEM-BSE images, however, it is still difficult to find an area as large as the ones imaged with SEM since the sample thickness is irrelevant for SEM-BSE but not for STEM. Fig. 6 (d) displays in general the difference of observable area between the TEM-based methods and SEM-based methods for the same electropolished AA7075 disc. Both TEM bright-field and HAADF-STEM need to collect electrons passing through the sample, which requires a thickness limit of less than a few hundred nanometers. The SEM imaging, in contrast, does not have this limitation. In other words, for normal bulk sample, the signal can always be captured from the interaction volume within the information depth without image degradation. This main difference between the two techniques explains the important observable area difference. As shown in Fig. 6(d), the area circled in dash line suitable for SEM observation is about 900 times larger than the 5 µm band (empirically estimated) enclosed in the white ellipse suitable for TEM or STEM imaging. Besides, the electropolishing success rate is much lower for TEM sample preparation than SEM. An under-etched or over-etched sample without any observable area for TEM can still be suitable for the proposed SEM imaging method. Insufficient observation area in TEM or STEM leads to more sample preparation time in order to obtain as many measurements as those performed with SEM-BSE. The advantage of SEM-BSE with the perspective of normal top view is more significant if numerous acquisitions are needed for data analytics.

3.3 GBPs measurements and SCC results

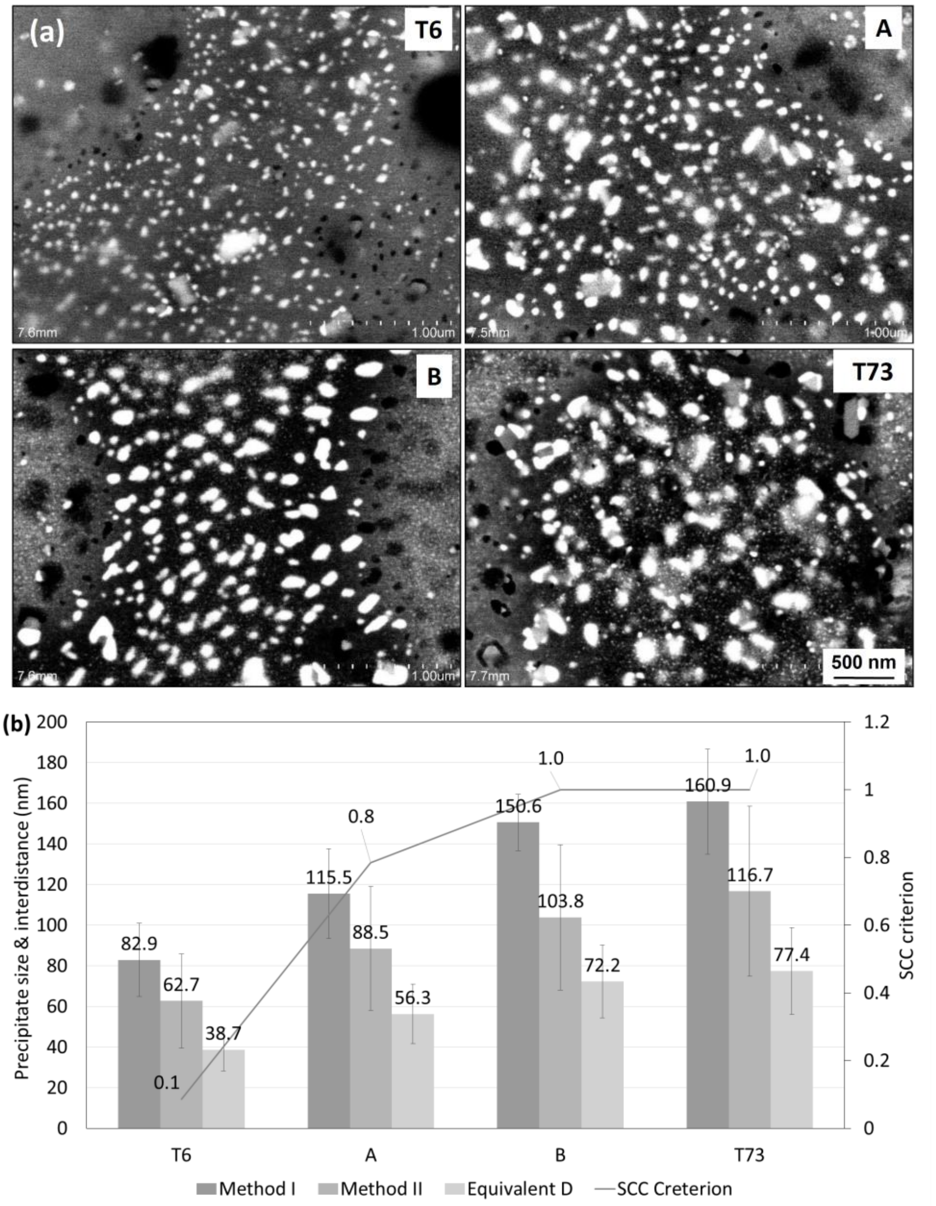

Fig. 7 (a) SEM-BSE images of the four AA7075 samples with the perspective of normal top view. (b) Measurements of GBPs size and inter-distance vs SCC criterion.

The measurements of GBPs size and inter-distance were performed respectively on four AA7075 samples with the heat treatment of T6, T73, A, and B (Table 1). The purpose of temper-A and temper-B is to mimic the standard aging T6 and T73 respectively while spending much lower treatment time. With higher temperature (177℃ vs 120℃) but shorter aging time, temper-A has rendered the AA7075 with a slightly over aged state compared to T6, with larger precipitates at the grain boundary, shown in Fig. 7(a). Temper-B, by applying a similar multi-step aging strategy with higher temperature, has also successfully aged the sample to be similar to the microstructure of the sample undergone T73 temper. Both T73 and temper-B are over aged state and are expected to show similar SCC resistance, better than T6 and Temper-A.

Two methods to evaluate the GBPs inter-distance were applied and compared. The method I denotes the measurements from lateral view from SEM. This is different from the parallel lateral view because the electron beam does not need to be parallel to the grain boundary while only one line of precipitates close to the surface is clearly shown in the image (Fig. 2(b)). As mentioned previously, the average spacing between GBPs was obtained in one direction along the intersection of the grain boundary and the imaging plane. The method II denotes the measurements of the nearest neighbor distance of GBPs within grain boundaries close to the polishing plane with the perspective of normal top view (Fig. 7(a)). To generate more reliable measurements for method II, the grain boundary areas acquired are with around 3 μm diameters.

Results shown in Fig. 7(b) demonstrate the GBPs inter-distance and spherical equivalent diameters share the same tendency: T6 < temper-A < temper-B < T73, where temper B and T73 samples have close values. The similar trend of measurements for GBPs inter-distance with both method I and method II using SEM indicates that we can choose either method to measure the average of precipitates spacing. As mentioned above, a larger quantity of measurements can be obtained with method II since it is with a two-dimensional region of precipitates to measure while only one line of precipitates are measured with method I. For the same reason, the results of nearest neighbor inter-distance generated with method II are systematically smaller than surface precipitates inter-distance measured with method I. In fact, the normal top view provided images (method II) can also serve for precipitate spacing measurements in one direction since we already have the two-dimensional information. The two-dimensional representation of GBPs opens the door to further modeling of corrosion behavior in correlation with PFZ structure, notably GBPs size and inter-distance.

The SCC resistance results measured with U-bend test are also shown in Fig. 7(b). The SCC criterion is calculated as follow:

$$SCC_{crit} = \frac{c_i}{c_t}$$

, where c_i is the number of cycles at failure and c_t is the total duration of the test. In the case where a specimen shows no sign of SCC for the whole duration of the test, it is assumed that $c_i > c_t$ and a value of 1 is attributed to the specimen. The results presented in Fig. 7(b) indicate that the SCC resistance of the 4 tempers follows a similar trend as the GBPs size and inter-distance: T6 < temper-A < temper-B ≈ T73.

It has been discussed in the literature (Kannan & Raja, 2006) that inter-granular cracking induced by the dissolution of continuously distributed anodic precipitates at the grain boundary (GBPs), typically at peak aging condition, is the main mechanism controlling the SCC susceptibility of these alloys. Over aged specimens are less affected by this phenomenon because the GBPs are coarser and more distant. The results shown in Fig. 7(b) confirm that peak aged specimen (T6) as well as the slightly over aged temper-A specimen are susceptible to this form of corrosion while the over aged T73 and temper-B specimen shows no sign of cracking. Fig. 7(b) also indicates that the SCC susceptibility of the different tempers roughly correlates with the GBPs inter-distance.

Moreover, it is worth mentioning that even if the T6 specimen GBPs are closer to each other than in the over aged tempers, their distribution is not continuous in the SEM-BSE images. Therefore it is highly likely that the continuity of the GBPs reported (Kannan & Raja, 2006), similar to Fig. 2(a), was only the projection of many precipitates overlapping for a certain thickness. In addition, according to the EDS results shown in Fig. S2 (details in supporting information), the composition of the PFZ matrix and GBPs after aging are close among four samples. It is unclear the influence of the chemical compositions of GBPs on SCC susceptibility. More spectra are needed to study their quantitative correlation, which is beyond the scope of this study.

4. Conclusions

In the current study, four samples of AA7075 with different aging histories (T6, A, T73 and B) were analyzed with SEM and TEM. The imaging methods were compared in detail to measure the size and inter-distance of GPBs. We successfully conducted imaging experiments with the perspective of normal top view for grain boundaries, and optimized the SEM-BSE imaging acceleration tension for GBPs analysis. Monte-Carlo simulations were performed to understand the visibility of precipitates with respect to calculated information depth. Finally, we applied the GBPs analysis results acquired from the reported SEM imaging method to validate the correlation between the GBPs structure and SCC resistance. The important findings are listed below.

1. The conventional parallel lateral view of PFZ for AA7075 with TEM is ineffective for GBPs inter-distance measurements due to its small observation area, overlapping effect and undesired diffraction contrast.
2. SEM-BSE imaging is an excellent alternative to TEM regarding the observation of grain boundary microstructures in AA7075. At around 10kV acceleration voltage, namely an information depth of 330 nm from the surface, ample area of grain boundaries quasi-parallel to the surface was frequently found in each sample. With more representative GBPs size and inter-distance measurements, it is highly recommended that the reported method using SEM-BSE observation with the perspective of normal top view should serve as a prior imaging method for AA7075 grain boundary and further data analytics.
3. HAADF-STEM can improve the image quality for the observation of grain boundaries in AA7075 compared to TEM bright-field, but it still lacks proper sampling area compared to SEM-BSE with the perspective of normal top view.

The SCC resistance ranking of AA7075 samples undergone four tempers is T6 < temper-A < temper-B ≈ T73. The SEM-BSE imaging with the perspective of normal top view succeeded in providing GBPs size and inter-distance measurements consistent with SCC results.

Acknowledgements

The study is supported financially by National Research Council of Canada.

Conflict of interest

The authors declare no potential conflict of interest.

Ajay Krishnan, M., Raja, V. S., Shukla, S., & Vaidya, S. M. (2018). Mitigating Intergranular Stress Corrosion Cracking in Age-Hardenable Al-Zn-Mg-Cu Alloys. *Metallurgical and Materials Transactions A: Physical Metallurgy and Materials*

Science, *49*(6), 2487–2498. https://doi.org/10.1007/s11661-018-4601-8

Assa'd, A. M. D., & Gomati, M. M. El. (1998). Backscattering Coefficients for Low Energy Electrons. *ECM Journal*, *12*(1), 185. https://www.ecmjournal.org/journal/smi/pdf/smi98-19.pdf

Berg, L. ., Gjønnes, J., Hansen, V., Li, X. ., Knutson-Wedel, M., Waterloo, G., Schryvers, D., & Wallenberg, L. . (2001). GP-zones in Al–Zn–Mg alloys and their role in artificial aging. *Acta Materialia*, *49*(17), 3443–3451. https://doi.org/10.1016/S1359-6454(01)00251-8

Birbilis, N., & Buchheit, R. G. (2005). Electrochemical Characteristics of Intermetallic Phases in Aluminum Alloys: An Experimental Survey and Discussion Electrochemical Characteristics of Intermetallic Phases in Aluminum Alloys An Experimental Survey and Discussion. *Iopscience.Iop.Org*, *152*(4), B140. https://doi.org/10.1149/1.1869984

Bobby-Kannan, M., Raja, V. S., Raman, R., & Mukhopadhyay, A. K. (2003). Influence of multistep aging on the stress corrosion cracking behavior of aluminum alloy 7010. *Corrosion*, *59*(10), 881–889. https://doi.org/10.5006/1.3287709

Burns, J. T., Kim, S., & Gangloff, R. P. (2010). Effect of corrosion severity on fatigue evolution in Al-Zn-Mg-Cu. *Corrosion Science*, *52*(2), 498–508. https://doi.org/10.1016/j.corsci.2009.10.006

Deshpande, N. U., Gokhale, A. M., Denzer, D. K., & Liu, J. (1998). Relationship between fracture toughness, fracture path, and microstructure of 7050 aluminum alloy: Part I. Quantitative characterization. *Metallurgical and Materials Transactions A*, *29*(4), 1191–1201. https://doi.org/10.1007/s11661-998-0246-3

Drouin, D., Couture, A. R., Joly, D., Tastet, X., Aimez, V., & Gauvin, R. (2007). CASINO V2.42 - A fast and easy-to-use modeling tool for scanning electron microscopy and microanalysis users. *Scanning*, *29*(3), 92–101. https://doi.org/10.1002/sca.20000

Frank, L., Steklý, R., Zadražil, M., El-Gomati, M. M., & Müllerová, I. (2000). Electron backscattering from real and in-situ treated surfaces. *Mikrochimica Acta*, *132*(2–4), 179–188. https://doi.org/10.1007/s006040050060

Ghosh, A., Ghosh, M., Seikh, A. H., & Alharthi, N. H. (2020). Phase transformation and dispersoid evolution for Al-Zn-Mg-Cu alloy containing Sn during homogenisation. *Journal of Materials Research and Technology*, *9*(1), 1–12. https://doi.org/10.1016/j.jmrt.2019.08.055

Goswami, R., Lynch, S., Holroyd, N. J. H., Knight, S. P., & Holtz, R. L. (2013). Evolution of grain boundary precipitates in Al 7075 upon aging and correlation with stress corrosion cracking behavior. *Metallurgical and Materials Transactions A: Physical Metallurgy and Materials Science*, *44*(3), 1268–1278. https://doi.org/10.1007/s11661-012-1413-0

Huang, L., Chen, K., & Li, S. (2012). Influence of grain-boundary pre-precipitation and corrosion characteristics of inter-granular phases on corrosion behaviors of an Al–Zn–Mg–Cu alloy. *Materials Science and Engineering: B*, *177*(11), 862–868. https://doi.org/10.1016/j.mseb.2012.04.008

Kairy, S. K., Turk, S., Birbilis, N., & Shekhter, A. (2018). The role of microstructure and microchemistry on intergranular corrosion of aluminium alloy AA7085-T7452. *Corrosion Science*, *143*, 414–427. https://doi.org/10.1016/j.corsci.2018.08.033

Kanaya, K., & Okayama, S. (1972). Penetration and energy-loss theory of electrons in solid targets. *Journal of Physics D: Applied Physics*, *5*(1), 43–58. https://doi.org/10.1088/0022-3727/5/1/308

Kannan, M. B., & Raja, V. S. (2006). Hydrogen embrittlement susceptibility of over aged 7010 Al-alloy. *Journal of Materials Science*, *41*(17), 5495–5499. https://doi.org/10.1007/s10853-006-0287-1

Kannan, M. B., Raja, V. S., & Mukhopadhyay, A. K. (2004). Determination of true stress corrosion cracking susceptibility index of a high strength Al alloy using glycerin as the non-corrosive atmosphere. *Scripta Materialia*, *51*(11), 1075–1079. https://doi.org/10.1016/j.scriptamat.2004.08.002

Knight, S. P., Birbilis, N., Muddle, B. C., Trueman, A. R., & Lynch, S. P. (2010). Correlations between intergranular stress corrosion cracking, grain-boundary microchemistry, and grain-boundary electrochemistry for Al–Zn–Mg–Cu alloys. *Corrosion Science*, *52*(12), 4073–4080. https://doi.org/10.1016/j.corsci.2010.08.024

Knight, S. P., Pohl, K., Holroyd, N. J. H., Birbilis, N., Rometsch, P. A., Muddle, B. C., Goswami, R., & Lynch, S. P. (2015). Some effects of alloy composition on stress corrosion cracking in Al–Zn–Mg–Cu alloys. *Corrosion Science*, *98*, 50–62. https://doi.org/10.1016/j.corsci.2015.05.016

Kumar, A., Godasu, A. K., Pal, K., & Mula, S. (2018). Effects of in-process cryocooling on metallurgical and mechanical properties of friction stir processed Al7075 alloy. *Materials Characterization*, *144*(August), 440–447. https://doi.org/10.1016/j.matchar.2018.08.001

Kumar, A., Pal, K., & Mula, S. (2017). Simultaneous improvement of mechanical strength, ductility and corrosion resistance of stir cast Al7075-2% SiC micro- and nanocomposites by friction stir processing. *Journal of Manufacturing Processes*, *30*, 1–13. https://doi.org/10.1016/j.jmapro.2017.09.005

Kumar, A., Pal, K., & Mula, S. (2021). Effects of cryo-FSP on metallurgical and mechanical properties of stir cast Al7075–SiC nanocomposites. *Journal of Alloys and Compounds*, *852*, 156925. https://doi.org/10.1016/j.jallcom.2020.156925

Liu, S. D., Chen, B., Li, C. B., Dai, Y., Deng, Y. L., & Zhang, X. M. (2015). Mechanism of low exfoliation corrosion resistance due to slow quenching in high strength aluminium alloy. *Corrosion Science*, *91*, 203–212. https://doi.org/10.1016/j.corsci.2014.11.024

Mondolfo, L. F. (1971). Structure of the aluminium: magnesium: zinc alloys. *Metallurgical Reviews*, *16*(1), 95–124. https://doi.org/10.1179/mtlr.1971.16.1.95

Mullerova, I., & Frank, L. (2003). Scanning low-energy electron microscopy. In *Advances in imaging and electron physics* (Vol. 128, pp. 310–445).

Niedrig, H., & Rau, E. . (1998). Information depth and spatial resolution in BSE microtomography in SEM. *Nuclear Instruments and Methods in Physics Research Section B: Beam Interactions with Materials and Atoms*, *142*(4), 523–534.

https://doi.org/10.1016/S0168-583X(98)00318-8

Peng, G., Chen, K., Chen, S., & Fang, H. (2011). Influence of repetitious-RRA treatment on the strength and SCC resistance of Al–Zn–Mg–Cu alloy. *Materials Science and Engineering: A*, *528*(12), 4014–4018. https://doi.org/10.1016/j.msea.2011.01.088

PiŇos, J., MikmekovÁ, & Frank, L. (2017). About the information depth of backscattered electron imaging. *Journal of Microscopy*, *266*(3), 335–342. https://doi.org/10.1111/jmi.12542

Polmear, I., St. John, D., Nie, J. F., & Qian, M. (2017). Light Alloys: Metallurgy of the Light Metals: Fifth Ed. In *Light Alloys: Metallurgy of the Light Metals: Fifth Edition*.

Prabhuraj, P., Rajakumar, S., Lakshminarayanan, A. K., & Balasubramanian, V. (2017). Evaluating stress corrosion cracking behaviour of high strength AA7075-T651 aluminium alloy. *Journal of the Mechanical Behavior of Materials*, *26*(3–4), 105–112. https://doi.org/10.1515/jmbm-2017-0019

Rau, E. I., & Reimer, L. (2001). Fundamental problems of imaging subsurface structures in the backscattered electron mode in scanning electron microscopy. *Scanning*, *23*(4), 235–240. https://doi.org/10.1002/sca.4950230403

Richards, R. G., Wieland, M., & Textor, M. (2000). Advantages of stereo imaging of metallic surfaces with low voltage backscattered electrons in a field emission scanning electron microscope. *Journal of Microscopy*, *199*(2), 115–123. https://doi.org/10.1046/j.1365-2818.2000.00717.x

Starink, M. J. (2001). Effect of compositional variations on characteristics of coarse intermetallic particles in overaged 7000 aluminium alloys. *Materials Science and Technology*, *17*(11), 1324–1328. https://doi.org/10.1179/026708301101509449

Ünlü, N. (2008). Preparation of high quality Al TEM specimens via a double-jet electropolishing technique. *Materials Characterization*, *59*(5), 547–553. https://doi.org/10.1016/j.matchar.2007.04.003

Zhou, L., Chen, K., Chen, S., Ding, Y., & Fan, S. (2021). Correlation between stress corrosion cracking resistance and grain-boundary precipitates of a new generation high Zn-containing 7056 aluminum alloy by non-isothermal aging and re-aging heat treatment. *Journal of Alloys and Compounds*, *850*, 156717. https://doi.org/10.1016/j.jallcom.2020.156717

Zhu, Y., Ophus, C., Toloczko, M. B., & Edwards, D. J. (2018). Towards bend-contour-free dislocation imaging via diffraction contrast STEM. *Ultramicroscopy*, *193*, 12–23. https://doi.org/10.1016/j.ultramic.2018.06.001

Figures

Fig. 1 Scheme of perspectives with normal top view and parallel lateral view to observe grain boundaries.

Fig. 2 (a) TEM image of GBPs of AA7075 at T6 temper from parallel lateral view. (b) SEM-BSE image of GBPs of AA7075 at T6 temper from lateral view.

Fig. 3 Grain boundary microstructure of AA7075 with T73 temper under TEM with a step-by-step tilt.

Fig. 4 (a) Depth distribution function of electron hits at 10kV. (b) Simulated BSE signal depth as a function of acceleration tension. (c) SEM-BSE images showing visibility vs. acceleration tension.

Fig. 5 SEM-BSE image (a) and illustration (b) of a concave grain boundary with ID at 10 kV.

Fig. 6 (a)TEM bright-field (b)SEM-BSE and (c)HAADF-STEM image of AA7075 grain boundary at T73 temper with perspectives close to normal top view; (d) SEM image of 3 mm diameter AA7075 disc at T73 temper with an electropolished hole of 485 × 355 µm, demonstrating the difference of observable area between TEM and SEM for the same sample.

Fig. 7 (a) SEM-BSE images of the four AA7075 samples with the perspective of normal top view. (b) Measurements of GBPs size and inter-distance vs SCC criterion.